sustainability

MDPI

Article

Numerical Investigation of Jet-Propelled Multiple-Vehicle Hyperloop System Considering the Suspension Gap †

Seraj Alzhrani *, Mohammed M. Abdulla, Khalid Juhany and Ibraheem AlQadi

Department of Aerospace Engineering, King Abdulaziz University, Jeddah 21589, Saudi Arabia; mabdullamohammed@stu.kau.edu.sa (M.M.A.); khalid@kau.edu.sa (K.J.); ialqadi@kau.edu.sa (I.A.).

* Correspondence: soalzahrani@kau.edu.sa

† This article is a revised and expanded version of a conference paper entitled "Effect of Maglev Suspension on the Aerodynamics of Multiple Vehicles Moving in a Low-Pressure Tube" which was presented at International Conference on Mechanical, Aerospace and Electronic Systems (MAES 2023), Johannesburg, South Africa, 24–26 November 2023.

Abstract: The Hyperloop system offers revolutionary transportation, aiming for near-sonic speeds in a low-pressure environment. The aerodynamic design challenges of multiple vehicles in a confined tube remain largely unexplored, particularly regarding vehicle spacing and suspension gaps. This study investigates a jet-propelled, multi-vehicle Hyperloop system using Reynolds-Averaged Navier–Stokes (RANS) equations and the $k-\omega$ turbulence model. Analysis of suspension gaps and vehicle spacing on drag and thrust revealed that suspension gaps cause significant jet deflection, reducing effective thrust and increasing drag. It was found that vehicle suspension, with a 75 mm suspension gap, increased drag by 58% at Mach 0.7 compared to the unsuspended configuration. Meanwhile, smaller vehicle spacing ($X_v = 0.25L_v$) reduced the drag by up to 50%, enhancing system efficiency. The results emphasize the need to address the effect of jet deflection and optimize vehicle spacing for maximum energy savings. These findings offer valuable insights for enhancing aerodynamic performance in multi-vehicle Hyperloop systems.

Keywords: hyperloop; suspension effect; low-pressure tube; multiple vehicles; jet flow

Citation: Alzhrani, S. Abdulla, M.M.; Juhany, K.; AlQadi, I. Numerical Investigation of Jet-Propelled Multiple-Vehicle Hyperloop System Considering the Suspension Gap. *Sustainability* **2024**, *16*, 9465. https://doi.org/10.3390/su16219465

Academic Editors: Luca Cioccolanti, Jie Ma, Jingxu Chen and Xinlian Yu

Received: 10 September 2024
Revised: 14 October 2024
Accepted: 23 October 2024
Published: 31 October 2024

1. Introduction

The Hyperloop, a futuristic transportation concept promising near-sonic speeds through low-pressure tubes, has the potential to revolutionize travel and logistics. This revolutionary idea, first proposed by Jospeh Foa (1966) in his tube flight and Oster (1999) as evacuated tube transportation (ETT) [1,2], gained significant momentum in 2013 when Elon Musk reignited interest with his vision of a near-vacuum tube system propelling passenger pods at near-sonic speeds (Mach number, M = 0.99) [3]. By minimizing air resistance within these low-pressure tubes (100 Pa), the Hyperloop aims to achieve unprecedented levels of speed, efficiency, and sustainability, captivating researchers worldwide with its potential advantages in safety, cost effectiveness, and passenger comfort. However, realizing this ambitious vision requires overcoming significant hurdles, including technological complexities, safety considerations, commercial viability, and regulatory frameworks.

One of the key challenges lies in understanding the aerodynamic characteristics of high-speed vehicles operating within the confined, low-pressure environment of the Hyperloop tube. Unlike vehicles in open spaces, where aerodynamic drag increases significantly with speed [4], the Hyperloop leverages reduced air density to minimize drag and maximize efficiency. However, aerodynamic drag remains a crucial factor, influenced by the vehicle's speed, length, and blockage ratio ($\beta = A_v/A_{tube}$), where A_v is the vehicle cross-sectional area and A_{tube} is the tube cross-sectional area [4–10].

Furthermore, flow compressibility plays a significant role in the system's overall performance, particularly at high speeds. Compression and expansion waves generated by

the vehicle's movement within the confined tube can lead to significant pressure differences, resulting in pressure drag, which is the dominant drag component in such systems [10–13]. Understanding these complex aerodynamic interactions is crucial for optimizing Hyperloop vehicle design and ensuring the feasibility of this groundbreaking transportation technology.

Numerical investigations, such as [4,5,13,14], have demonstrated that the strength of the normal shock wave formed in front of the vehicle increases with both vehicle speed and β. Throrely and Tiley review theoretical and some experimental studies on unsteady and transient flow of compressible fluids in pipelines, with a focus on developing equations that consider wall friction and heat transfer, providing methods of solution for such flows [15]. Abdulla et al. used the method of characteristics to numerically investigate a high-speed object in a tube, observing the presence and propagation of compression and expansion waves within the tube system [7]. At near-transonic speeds, a complex system of shock waves, including oblique and trailing shocks, appears behind the moving object, significantly contributing to the total aerodynamic drag and potentially impacting system safety and feasibility [4,14].

The aerodynamic interactions become even more complex in a multi-vehicle Hyperloop system. The flow field around and behind each vehicle, including the propagation and interaction of compression and expansion waves, influences the overall aerodynamic performance. Additionally, the phenomenon of choking, where the flow reaches sonic conditions, can occur at high speeds and blockage ratios (e.g., 180 m/s and $\beta = 0.36$, as observed by Oh et al. [11]), leading to a substantial increase in drag.

To decrease the risks asociated with the very low pressure (100 Pa) in the Hyperloop system, the High-speed Transportation research group at King Abdulaziz University proposes a Hyperloop system with reduced pressure levels at 10,000 Pa, the vehicle operating by fan/compressor at the fore part of each moving vehicle (i.e., mitigating the Kantrowitz Limit). The first attempt to employ a fan/compressor was made by Lluesma-Rodrguez et al. [16], who performed comprehensive CFD simulations to study the power consumption of the Hyperloop operating system. The compressor was beneficial for reducing power consumption by around 70% [16]. Similarly, Kwon et. al reported that a reduction of 30% of the aerodynamic drag at 600 km/h could be achieved by using an air-breathing device at the front of the vehicle [17]. Bizzozero et al. proposed a concept of the vehicle utilizing a compressor with jet exit at its aft part to transfer the flow from the front to the rear part, which works as a thrust device to propel the vehicle [18].

Magnetic levitation (Maglev) is essential for the vehicle–tube system to levitate above the tracks and eventually eliminate the frictional resistance between the wheels and rails. Despite Musk's concept of using air bearings in levitation, as it needs massive pressure to maintain track clearance, an electromagnetic suspension system can extend the height more, which leads to an efficient and feasible system. Electromagnetic suspension, electrodynamic suspension, and high-temperature superconducting are the three major classifications of Maglev transportation technology [19].

Experimental work for Hyperloop technology is limited owing to high costs, a time-consuming process, and a lack of funds. Therefore, most current Hyperloop studies rely on numerous computational methods to investigate the flow field around the running vehicles and enhance the aerodynamic performance [5,8,11,13,16,17,20–29].

The Hyperloop technology has many limitations, but it has several unique advantages. Traveling from Jeddah to Riyadh in Saudi Arabia (i.e., the most demanded flight route) is estimated to be one hour and twenty minutes, with a maximum speed of 820 kph (M = 0.7) via airplanes. The Hyperloop system could transport passengers faster than an airplane with a favorable load/unload time. Airplanes have a turnaround time of more than one hour. However, the Hyperloop is an attractive option with high-speed boarding/departing time. If multiple vehicles are designed and tested, it could be like a subway train. A similar concept has been proposed by NEOM to be operated in the linear smart city—car free—"The Line" [30]. The study aligns with Saudi Arabia's Vision 2030, which emphasizes

infrastructure modernization, environmental sustainability, and economic diversification. Through the enhancement of energy efficiency and vehicle stability in Hyperloop systems, the research supports the development of innovative transportation solutions that reduce carbon emissions and contribute to sustainable high-speed transit. Jet propulsion offers an alternative to traditional propulsion methods, with the potential to minimize drag and improve efficiency in Hyperloop systems.

This research pioneers a comprehensive investigation into the aerodynamic performance of a jet-propelled, multi-vehicle Hyperloop system operating within a low-pressure tube [31]. Unlike conventional Hyperloop designs that rely on magnetic levitation, this study explores the potential of jet propulsion in a confined, low-pressure environment, offering a novel approach to sustainable high-speed transportation. In our previous work, we explored the aerodynamic performance of a multiple-vehicle system propelled by air-breathing jet propulsion in a low-pressure environment. The focus was on an axisymmetric model where vehicles equipped with an air-breathing propulsion system demonstrated significant improvements in aerodynamic performance over a single-vehicle system. Our analysis revealed that the air-breathing multiple-vehicle configuration could reduce drag by up to 57%, especially at closer vehicle-to-vehicle spacings, due to favorable flow interactions and propulsion benefits.

The role of suspension gaps is critical in maintaining stable flow fields between vehicles, preventing adverse flow separations and shock wave formations that would otherwise increase drag. Kim et al. examined the effects of pod misalignment, highlighting that precise spacing and suspension gap management are essential to avoid increases in drag due to flow disturbances [32]. Studies such as Zhong et al. also emphasized the importance of managing shock waves and pressure propagation in confined, high-speed environments, where improper suspension gaps can lead to increased flow disturbances and degrade performance [33]. Especially when the vehicle is equipped with a jet nozzle for propulsion, the flow structure is significantly affected [34,35].

The current research builds upon previous efforts [7,31,34–36] by investigating the impact of suspension gaps and utilizing 3D flow simulations to gain a deeper understanding of flow dynamics and aerodynamic challenges in a more realistic multi-vehicle Hyperloop system. A key focus is placed on how the suspension gap affects thrust and drag efficiency.

This work specifically addresses the underexplored area of suspension gaps in Hyperloop system aerodynamics. Through detailed numerical simulations using Reynolds-Averaged Navier–Stokes (RANS) equations and CFD techniques, the study examines the interactions between vehicle spacing, jet propulsion, and suspension dynamics in confined, low-pressure environments. The findings offer valuable insights for optimizing jet propulsion and improving overall system performance, contributing to more sustainable and efficient transportation solutions.

2. Numerical Simulation

2.1. Model Description

The system developed by the High-speed Transportation research group at King Abdulaziz University involves the operation of multiple vehicles within a low-pressure tube maintained at 10 kPa. This design is aimed at enhancing passenger and freight capacity. Each individual vehicle within the system is equipped with an air compressor and a jet exit mechanism to generate thrust as illustrated in Figure 1. To capture intermediate effects effectively, this study selects a minimal configuration of three vehicles, as the intermediate vehicle exhibits a similar flow field characteristic to the others. In this simulation, all multiple vehicles are identical as depicted in Figure 1. The tube's diameter is 5 m, while the individual vehicle's diameter is set at 3 m. This choice of dimensions results in a selected $\beta = 0.36$. This blockage ratio is widely recommended for optimizing the aero-structural aspects of Hyperloop systems [4,11,13,20]. Both the axisymmetric (centered) and the Maglev suspension gap effect are simulated at various vehicle-to-vehicle distance (X_v) at different Mach numbers (0.3 representing the performance at the lower subsonic flow

regimes, M = 0.5 for the moderate subsonic, and 0.7 representing the cruise condition). Due to the implementation of the air compressor, each vehicle produces a weak compression wave and jet expansion at the end [36]. The reason for using the vehicle-to-vehicle distance as a parameter is to study the effect on the aerodynamics and the flow field. The suspension gap study aims to avoid the axisymmetric assumption for the realistic model where Maglev technology is used. The suspension gap effect on the aerodynamic characteristics was studied by Zhou et al. [33] and the effect of the Maglev train track was investigated by Hu et al. [22]. The establishment of vehicle-to-vehicle distance (X_v) and suspension gap (d) provides a better resolution to estimate the impact of these parameters on the performance of multiple vehicles equipped with the air compressor and the jet nozzle Hyperloop system as presented in Figure 2.

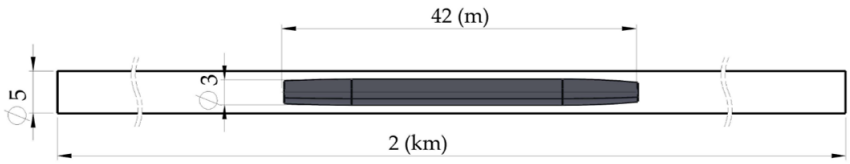

Figure 1. General configuration and major dimensions of the single-vehicle tube system.

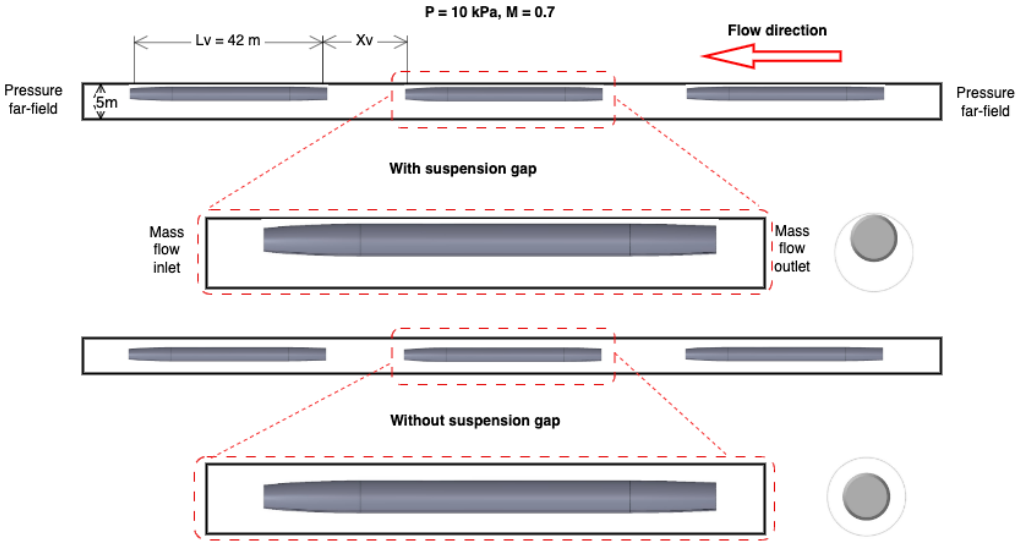

Figure 2. Model diagram of the multiple-vehicle tube system (axisymmetric and suspension) and boundary conditions.

2.2. Flow Regimes

The flow physics in a Hyperloop system are primarily governed by two key parameters: Reynolds number and Mach number. The flow field is characterized by a moderate Reynolds number, Re = 1.9×10^6. Three vehicle speeds are explored through varying Mach numbers: low subsonic (0.3), medium subsonic (0.5), and high subsonic (0.7). Additionally, the compressor pressure ratio and jet exit velocity also influence the flow field. The "Kantrowitz limit" (choked flow at supersonic or transonic velocities) and the piston effect (high-pressure region forming in front of the vehicle) are critical flow behaviors that impact system performance [24].

Due to the low operating pressure, the Knudsen number (Kn) is relevant. To ensure the validity of the continuum assumption, Kn should be less than 0.001. Based on the Reynolds number and vehicle Mach number, the calculated Knudsen number is 5.4×10^{-5}, satisfying the continuum assumption.

As described in Figure 3, the flow field is altered by the impact of the following vehicle, the compression waves (CW) accumulated in the front of the vehicles, and expansions (EW) occur at the last vehicle fore. The interaction region is presented between each vehicle.

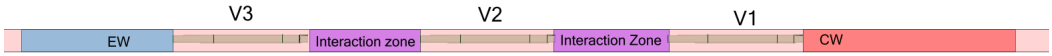

Figure 3. Pressure flow field of multiple vehicles moving a tube. V_1, V_2 and V_3 are first, second, and last running vehicle.

2.3. Limitation and Assumptions

- The RANS modeling approach used in this study does not fully capture transient wake effects and flow disturbances such as vortex shedding and wake interference between vehicles, which may lead to an underestimation of drag forces and flow instability in the confined Hyperloop environment.

Several simplifications were made in this study to streamline the computational analysis of jet-propelled vehicles in the Hyperloop system.

- First, the flow is assumed to be in a continuum mode, which is valid for low-pressure environments since Kn < 0.001 as provided in Section 2.2.
- Second, a constant mass flow rate is assumed across all vehicles, ignoring potential variability in propulsion performance and jet flow interactions, which could lead to fluctuations in thrust and drag. While necessary for reducing complexity, these assumptions may limit the model's accuracy in capturing localized flow phenomena and transient behaviors.

2.4. Governing Equations

The flow field around the multiple vehicles in the Hyperloop system is governed by the compressible Reynolds-Averaged Navier–Stokes (RANS) equations along with the $k-\omega$ SST turbulence model. The continuity, momentum, and energy equations are given as follows:

The continuity equation for the conservation of mass is expressed as

$$\frac{\partial \rho}{\partial t} + \frac{\partial (\rho \overline{u_i})}{\partial x_i} = 0 \tag{1}$$

where ρ is the fluid density and $\overline{u_i}$ is the time-averaged velocity component in the i direction. The RANS form of the momentum equation is given by

$$\frac{\partial (\rho \overline{u_i})}{\partial t} + \frac{\partial (\rho \overline{u_i u_j})}{\partial x_j} = -\frac{\partial \overline{p}}{\partial x_i} + \frac{\partial}{\partial x_j}\left[\mu\left(\frac{\partial \overline{u_i}}{\partial x_j} + \frac{\partial \overline{u_j}}{\partial x_i} - \frac{2}{3}\delta_{ij}\frac{\partial \overline{u_k}}{\partial x_k}\right)\right] - \frac{\partial \overline{\tau_{ij}}}{\partial x_j} \tag{2}$$

where $\overline{p}$ is the mean pressure, μ is the dynamic viscosity, and $\overline{\tau_{ij}} = \rho \overline{u_i' u_j'}$ represents the Reynolds stress tensor. The conservation of energy equation, which includes the turbulent heat flux, is expressed as

$$\frac{\partial (\rho \overline{e})}{\partial t} + \frac{\partial (\rho \overline{e u_j})}{\partial x_j} = \frac{\partial}{\partial x_j}\left[(k + k_t)\frac{\partial \overline{T}}{\partial x_j}\right] + \overline{u_i}\frac{\partial \overline{p}}{\partial x_i} + \tau_{ij}\frac{\partial \overline{u_i}}{\partial x_j} - \frac{\partial}{\partial x_j}\left(\rho \overline{u_i' h'}\right) \tag{3}$$

where $\overline{e}$ is the total energy per unit mass, k is the thermal conductivity, k_t is the turbulent thermal conductivity, $\overline{T}$ is the mean temperature, and $\rho \overline{u_i' h'}$ represents the turbulent heat flux.

2.5. Turbulence Model

The high-speed vehicle–tube system was studied and analyzed numerically in numerous research works [8,11,13,16,20–29]. The $k-\epsilon$ turbulence model was applied by

Chen et al. [37]. Most of the works use the $k-\omega$ turbulence model with the axisymmetric assumption, for example, works of [5,11,13,17,20,21]. Later, IDDES (Improved Delayed Detached Eddy Simulation) with the RANS region resolved with the $k-\omega$ for a small-scaled Hyperloop model was utilized to reduce the computational budget [22]. Zhou et al. employed the SAS model (Scale Adaptive Simulation) for the analysis of radial gap effect on aerothermal performance of a transonic Hyperloop [29].

The $k-\omega$ SST (Shear Stress Transport) model is a widely used turbulence model in computational fluid dynamics due to its ability to accurately capture complex flow behaviors such as adverse pressure gradients and flow separation. These characteristics are particularly crucial in high-speed applications such as Hyperloop systems. Introduced by Menter [38], the model integrates the strengths of the $k-\omega$ formulation in the near-wall region with the $k-\epsilon$ model in free shear flows, offering robust predictions across a wide range of flow regimes. The effectiveness of the $k-\omega$ SST model has been validated in numerous studies focused on Hyperloop systems, consistently demonstrating its capability to analyze the aerodynamic performance and flow characteristics of high-speed vehicles within low-pressure tubes. This study employs the default parameter values of the $k-\omega$ SST model. The Turbulent Kinetic Energy (k) Equation is expressed as follows:

$$\frac{\partial(\rho k)}{\partial t}+\frac{\partial(\rho k\overline{u_j})}{\partial x_j}=\tau_{ij}\frac{\partial\overline{u_i}}{\partial x_j}-\beta^*\rho\omega k+\frac{\partial}{\partial x_j}\left[(\mu+\sigma_k\mu_t)\frac{\partial k}{\partial x_j}\right] \tag{4}$$

The Specific Dissipation Rate (ω) Equation is expressed as follows:

$$\begin{aligned}\frac{\partial(\rho\omega)}{\partial t}+\frac{\partial(\rho\omega\overline{u_j})}{\partial x_j}=&\frac{\gamma}{\nu_t}\tau_{ij}\frac{\partial\overline{u_i}}{\partial x_j}-\beta\rho\omega^2+\frac{\partial}{\partial x_j}\left[(\mu+\sigma_\omega\mu_t)\frac{\partial\omega}{\partial x_j}\right]\\&+2\rho(1-F_1)\sigma_{\omega2}\frac{1}{\omega}\frac{\partial k}{\partial x_j}\frac{\partial\omega}{\partial x_j}\end{aligned} \tag{5}$$

The default constants for the $k-\omega$ SST model are

$$\begin{aligned}&\sigma_{k1}=0.5,\quad \sigma_{\omega1}=0.5,\quad \beta_1=0.0750\\&\sigma_{k2}=1.0,\quad \sigma_{\omega2}=0.856,\quad \beta_2=0.0828\\&\beta^*=0.09,\quad \kappa=0.41,\quad \gamma_1=\frac{\beta_1}{\beta^*}-\frac{\sigma_{\omega1}\kappa^2}{\sqrt{\beta^*}},\quad \gamma_2=\frac{\beta_2}{\beta^*}-\frac{\sigma_{\omega2}\kappa^2}{\sqrt{\beta^*}}\end{aligned}$$

The $k-\omega$ SST model utilizes blending function F_1 defined based on the distance from the wall to transition smoothly between the $k-\omega$ and $k-\epsilon$ models. These constants ensure accurate predictions of complex flow behaviors such as adverse pressure gradients and flow separation, especially in high-speed aerodynamic applications [38].

In this study, RANS simulations were performed using the finite-volume method of CFD software FLUENT 19.3. Spatial discretization employed a second-order upwind scheme [39]. The inviscid flux was calculated using the ROE scheme [40], and the Least Square Method [41] was used for spatial gradient discretization. The momentum and energy terms were discretized using the second-order upwind scheme [39]. The computational domain was extended to ensure fully developed flow. All numerical simulations were performed using the HPC AZIZ facility [42].

2.6. Grid Generation Approach

A hexahedral structured mesh was employed to discretize the computational domain. To determine the appropriate grid size, three types of grid densities (coarse, medium, and fine) were generated, as shown in Figure 4, for the case of $X_v = 0.5L_v$. The grid sizes on the vehicle for coarse, medium, and fine densities were 30 mm, 15 mm, and 5 mm, respectively, with total grid counts of 2.55, 8.6, and 15.3 million cells, respectively. For all three grid densities, the height of the first boundary layer grid was approximately 0.01 mm with a

growth rate of 1.1 to simulate the near-wall flow field and maintain $y^+ \approx 5$, as shown in Figure 4. The same grid strategy was adopted for both suspended and centered vehicles using medium grid levels.

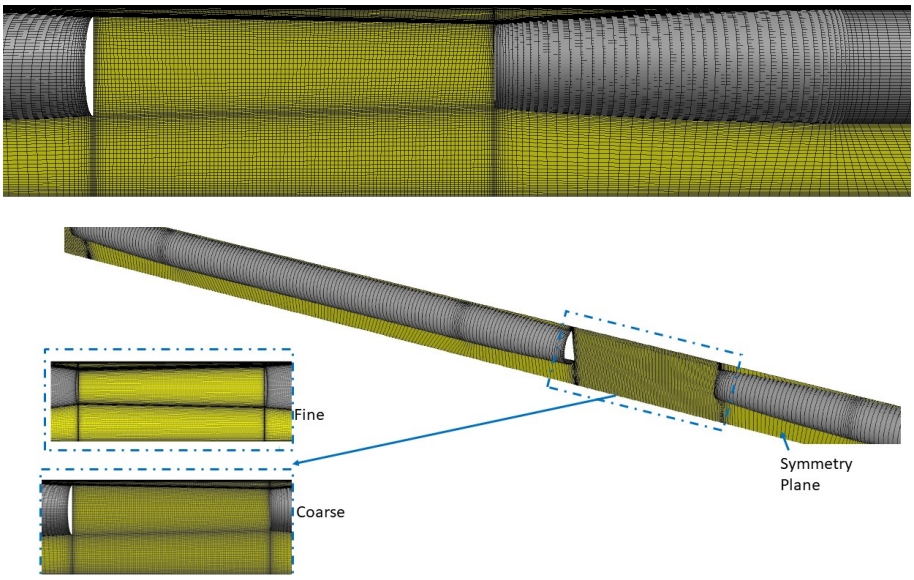

Figure 4. Three-dimensional supended model: grid and boundaries.

2.7. Boundary Conditions

The pressure far field boundary type is employed on the tube portal, following the methodology of Niu et al. [14,29]. At the jet exit face, a mass flow inlet type is used, where the total temperature and mass flow rate are specified to determine the thrust force. The fan entrance is configured as a mass flow outlet. The mass flow rate and total temperature for the three Mach number regimes are detailed in Table 1.

Table 1. Vehicle inflow/outflow boundary conditions at different Mach numbers.

Mach Number	$\dot{m}$ (kg/s)	V_{jet} (m/s)	T_0 (K)
0.3	64	121	305
0.5	107	281	339
0.7	150	347	360

The cruise conditions of a vehicle are defined by constant speed and zero acceleration. To maintain force equilibrium in the direction of motion, the thrust force must equal the drag force. The initial specifications for the air-breathing system in this study used a specified mass flow rate based on a single-vehicle system configuration. However, this mass flow rate is insufficient to achieve force equilibrium in a multiple-vehicle system. To maintain force balance in the multiple-vehicle system, the thrust must be adjusted. This can be accomplished by using a variable RPM fan with a reduction gear to control the mass flow rate or by regulating the jet exit velocity through a centered-body system.

An iterative procedure was developed to determine the required mass flow rate to achieve force equilibrium. A User-Defined Function (UDF) is employed to calculate the drag force based on the results of the previous iteration, ensuring that the mass flow rate and total temperature match. The procedure is initialized using the values from Table 1. Subsequently, the required air-breathing mass flow rate by the compressor is increased or decreased to achieve force balance.

2.8. Grid Convergence and Validation

2.8.1. Grid Convergence Study

Three grid levels were examined in the scenario where $X_v = 0.5L_v$. The grid sizes on the vehicle for low, medium, and high densities are 30 mm, 15 mm, and 5 mm, respectively. The drag force results were computed and monitored for three vehicles, and the system's average drag for each grid level confirmed the convergence of the grid. Notably, the difference between the coarse and medium grids in the system's average drag is more pronounced compared to the fine grid. Consequently, the medium grid was employed for the remaining simulation cases with various configurations as shown in Table 2.

Table 2. Grid dependence check.

Grid Level	Grid Size	V_1		V_2		V_3		System Average	
		Drag (N)	Diff. %	Drag (N)	Diff. %	Drag (N)	Diff. %	Drag (N)	Diff. %
Coarse	2.55 M	3454	-	4500	-	22,036	-	9997	-
Medium	8.6 M	3481	0.78%	4539	0.85%	22,832	3.61%	10,284	2.87%
Fine	15.5 M	3466	0.46%	4513	0.57%	22,820	0.64%	10,266	0.17%

2.8.2. Validation with DLR Ejector Model

The DLR model of the hydrogen ejector is utilized to verify the numerical solution method specified in the previous section. The model dimensions and the boundary condition are defined in Figure 5. The inflow/outflow boundary types are the pressure far field, the hydrogen ejector specified to the mass flow inlet, and the top and bottom walls, which are stationary adiabatic walls as well as the model walls.

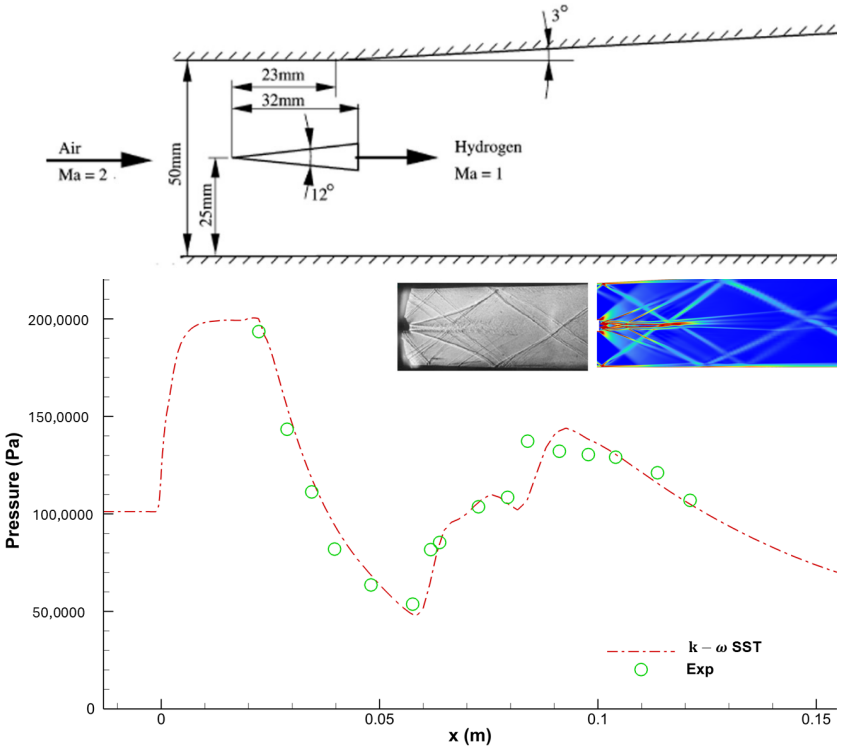

Figure 5. DLR ejector model dimensions, boundary conditions, computational grid, and pressure distribution on the bottom wall [43].

The quadrilateral element is used with a total number of elements around 140,000 cells. The maximum cell aspect ratio is 74 with near-wall distance around 0.005 mm corresponding to y+ around 1. The grid is constructed using ANSYS ICEM meshing tool. The flow

field Mach number is two with the inlet pressure of 200 kPa. The hydrogen ejector speed is 1200 m/s which is equivalent to M = 1 based on hydrogen properties.

Figure 5 depicts the pressure distribution at the bottom wall computed using the $k-\omega$ and the experimental results [43], which provided a good agreement. The pressure magnitude decreases downstream due to the presence of the complex diamond shock-cell structure along with the ejector and jet spread downstream. Both the numerical solution and experimental outcomes show this decrease in the pressure as the shock weaken downstream.

2.8.3. Validation with RAE 2822 Airfoil

The well-known case of the RAE 2822 airfoil under flight conditions of $M = 0.729$, $p = 15.8$ psi, $T = 460^{\circ}R$, and $\alpha = 2.31^{\circ}$ was employed to validate the current numerical approach using the $k-\omega$ turbulence model. The grid was generated using the ANSYS ICEM CFD meshing tool, utilizing 2D quadratic elements with near-wall spacing corresponding to $y^{+} \approx 1$. The grid around the airfoil consisted of 550 elements, while the computational domain extended 50 chord lengths upstream and downstream, resulting in a total of 198,000 elements. A pressure far-field boundary condition was applied at the inlet and outlet, and the airfoil surface was considered adiabatic.

This validation at transonic flow conditions, where a normal shock wave was accurately captured, is crucial for demonstrating the model's proficiency in simulating complex aerodynamic behaviors such as shock waves and pressure distributions. These capabilities are particularly relevant to this study, as they validate the model's accuracy in assessing the aerodynamic performance of jet-propelled vehicles in the Hyperloop system, where shock wave interactions, suspension effects, and jet flows significantly influence the flow physics in a confined low-pressure environment.

The comparison of the computed pressure coefficient distribution with experimental data [44] shows excellent agreement, as depicted in Figure 6, accurately capturing the minimum pressure coefficient and the precise shock wave location, thus confirming the reliability of the numerical scheme.

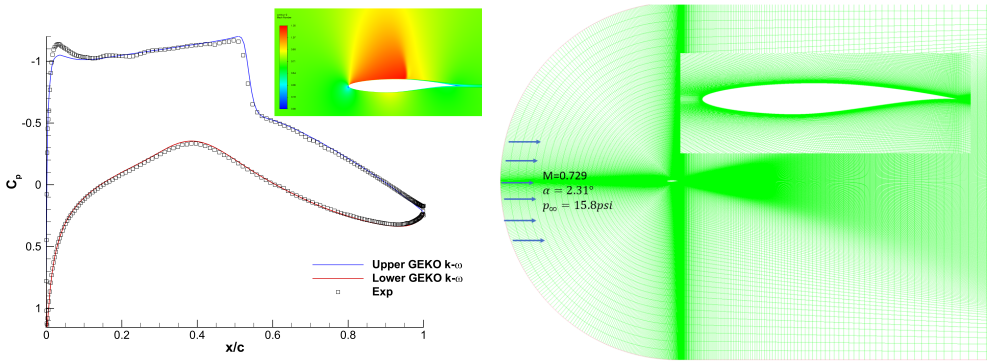

Figure 6. RAE 2822 validation case- pressure coefficient distribution over airfoil surface, arrows represent flow direction, (experimental data source: [44]).

2.8.4. Turbulence Model Effects

The case $X_v = L_v$ was utilized to verify the solution of the $k-\omega$ model using the medium grid. Similar boundary conditions were applied with the medium-sized grid level and solved using the $k-\omega$ SST, the one-equation SA (Spalart–Almaras) model [45], and $k-\epsilon$ Realizable models [46]. The results confirm the accuracy of the $k-\omega$ SST model when compared with the aforementioned turbulence models. The difference in drag force for the first vehicles (V_1, V_2) is negligible, while the drag force for the last vehicle (V_3) shows 2% and 1% differences from the $k-\omega$ SST and $k-\epsilon$ Realizable models, respectively, as presented in Table 3.

Table 3. Validation of $k-\omega$ SST model Vs SA and $k-\epsilon$ Realizable.

Turbulence Model	Vehcile 1		Vehicle 2		Vehicle 3	
	Drag	% Diff.	Drag	% Diff.	Drag	% Diff
$k-\omega$ SST	2705	———	3469	———	22,647	——
(SA)	2707	0.07%	3470	0.03%	22,170	2%
$k-\epsilon$ Realizable	2707	0.02%	3471	0.03%	22,401	1%

3. Results and Discussion

In this section, we present the results of our numerical simulations, focusing on the aerodynamic performance of a jet-propelled, multi-vehicle Hyperloop system. We highlight the influence of suspension gaps and vehicle spacing on the overall system performance, providing insights into the complex flow dynamics and interactions within the confined low-pressure tube. Our findings are discussed in detail, emphasizing the key observations and their implications for Hyperloop design and operation.

The simulation results for a single vehicle are presented first to establish a baseline for comparison. Analysis of the flow field around this vehicle includes the suspended and unsuspended cases. Subsequently, results for multiple axisymmetric and suspended vehicles at cruise conditions are examined. Pressure and Mach number contours illustrate the aerodynamic interactions at various vehicle-to-vehicle distances. The drag force variations with respect to Mach number and inter-vehicle spacing are tabulated and discussed. By comparing the average drag of the multi-vehicle configurations to that of the single-vehicle reference, the potential energy and power savings are quantified.

3.1. Single-Vehicle Aerodynamic Performance

The reference model for the current analysis is a 3D model of a single vehicle, both with and without a suspension gap. The suspension model was examined at a blockage ratio of $\beta = 0.36$ and Mach numbers of 0.3, 0.5, and 0.7.

3.1.1. Flow Structure Around the Vehicle

The static pressure contours and Mach number distribution at a cruise Mach number of 0.7 are illustrated in Figures 7 and 8, respectively, both at $p = 10$ kPa and $\beta = 0.36$. Figure 7 shows the static pressure distribution around the vehicle within the confined tube system. With the flow moving from right to left, higher pressure is observed in front of the vehicle, while lower pressure regions appear primarily at the rear of the vehicle.

Figure 8 depicts the Mach number contours. The flow accelerates as it approaches the vehicle, reaching its highest velocities ($\sim$1.5–2) in the confined space between the tube wall and the vehicle's body. The wake region to the left of the vehicle shows complex flow patterns, including shock waves and boundary layer interaction. The flow field appears vertically asymmetric, with different patterns visible in the upper and lower halves of the tube. These visualizations highlight significant flow acceleration around the vehicle and complex wake structures. The high Mach number regions and pressure variations, particularly around the vehicle's rear (leading edge) and in its wake, are critical areas for further investigation and potential design optimization to enhance system performance and stability.

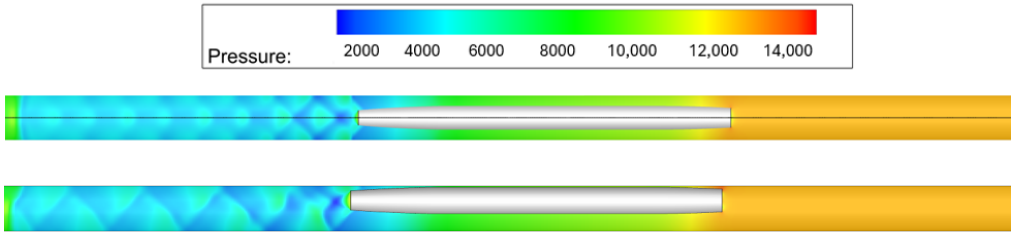

Figure 7. Static pressure contours at p = 10 kPa, $M = 0.7$, and $\beta = 0.36$.

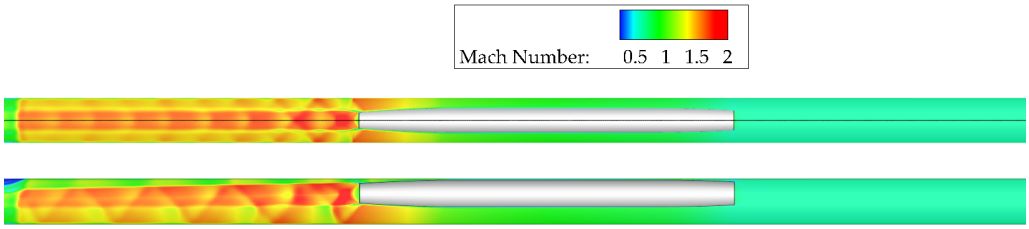

Figure 8. Mach number contours at p = 10 kPa, M = 0.7, $\beta = 0.36$.

3.1.2. Comparison of Centered and Suspended Single-Vehicle Models

Figure 9 illustrates the Mach number contours with their variation along the jet centerline and the tube walls. The data are shown for both the axisymmetric and suspended model flow fields around the rear of the vehicle.

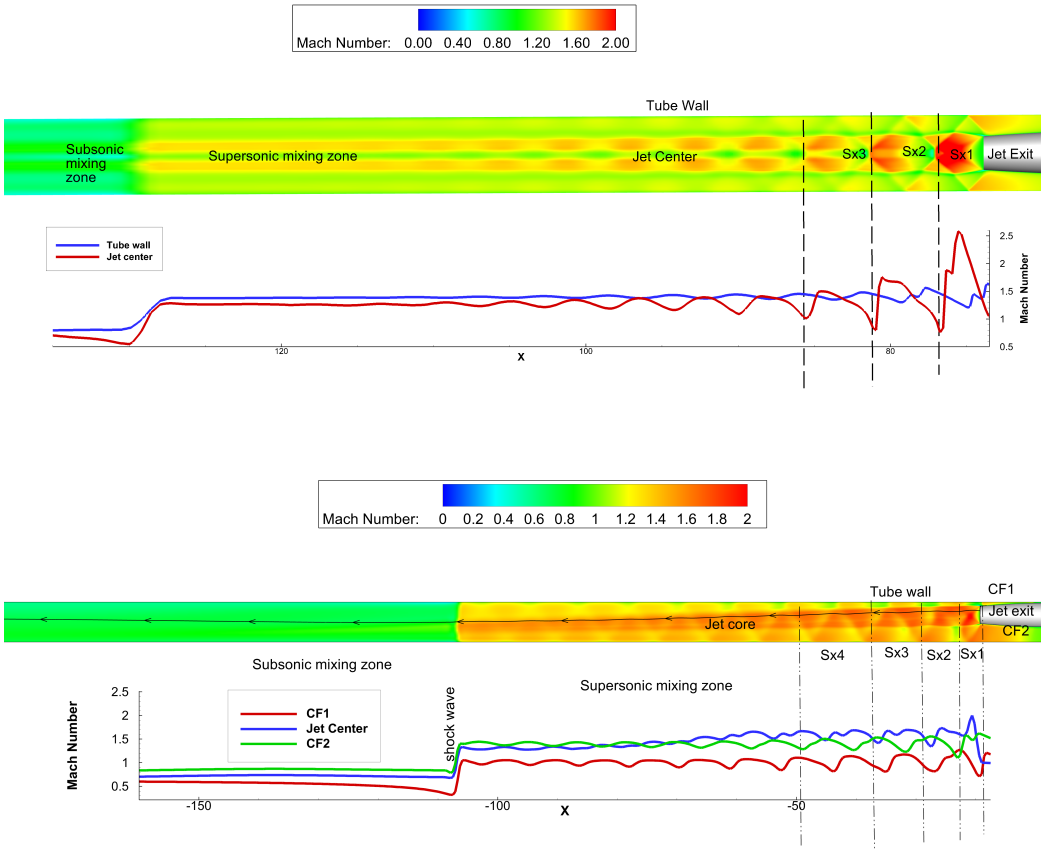

Figure 9. Mach number contours for axisymmetric and suspended models for the rear vehicle, x is distance downstream measured in m from system origin point, at $p = 10$ kPa, M = 0.7, $\beta = 0.36$.

In the axisymmetric model, the flow structure reveals a high-speed jet core emanating from the vehicle's rear, with Mach numbers peaking at the jet exit. Multiple strong shock waves (Sx1, Sx2, Sx3) are evident as sudden Mach number changes. The Mach number plot for the axisymmetric model shows relatively consistent values near the tube wall and jet center, with the flow near the wall maintaining supersonic speed.

The suspended model, however, exhibits notable differences. The primary distinction between the axisymmetric and suspended models is the downward deflection of the jet core in the suspended configuration. The Mach number plot reveals somewhat greater variation among CF1 (upper boundary) and CF2 (lower boundary) compared to the axisymmetric case. A strong terminating shock is visible around $x = -100$, where all three lines show a sudden Mach number decrease. The jet asymmetry reduces the effective thrust and generates an upward force, which exposes the vehicle to a pitching moment.

3.2. Axisymmetric Model of Multiple Moving Vehicles

This section addresses the axisymmetric configuration of a multiple-vehicle system (centered within the tube).

3.2.1. Flow Field Characteristics at Different Vehicle Spacings

In this analysis, the flow structure for the axisymmetric model (centered vehicle) without a suspension gap is examined.

Figure 10 highlights the flow field at a short spacing ($X_v = 0.25L_v$). At $X_v = 0.25L_v$, shock-free flow is observed around the leading and middle vehicles due to the compression wave generated by the following vehicle. This compression creates a favorable pressure gradient, allowing smoother flow and preventing the formation of shock waves. In essence, the trailing vehicle acts as a 'moving nozzle,' extending the flow passage for the leading vehicles. However, the trailing vehicle, lacking this proximity effect, experiences more complex shock and expansion waves, resulting in significant drag. The maximum Mach number at the oblique shock wave behind the trailing vehicle approaches two, with a 12 kPa pressure difference between the leading and trailing vehicles. This under-expanded jet creates high noise levels and potential structural damage.

Figure 11 presents the Mach number and static pressure contours for three vehicles—leading, middle, and trailing—at a larger spacing ($X_v = 2L_v$). The Mach number contours reveal the formation of weak shock waves around all three vehicles. The trailing vehicle experiences the most complex flow patterns, with a strong shock wave observed at its rear due to the adverse pressure gradient in this region. This strong shock leads to boundary layer separation and increased drag. The flow expands, increasing the Mach number to approximately 1.8, resulting in the formation of an under-expanded jet, though less intense than in the closer spacing configuration. Examining the pressure contours, more distinct pressure variations are observed around all vehicles. A significant pressure difference of about 12 kPa exists between the leading and trailing vehicles. The trailing vehicle exhibits a marked pressure differential between its front and rear, contributing to its increased drag. The middle and leading vehicles also show more pronounced pressure gradients, with higher pressures at their fronts (yellow) and lower pressures at their rears.

These observations support the concept that at larger spacings, each vehicle experiences more individual flow characteristics, leading to the formation of shock waves and increased overall system drag compared to the closer spacing configuration. The reduced influence of the trailing vehicle on the leading vehicles' flow fields results in less favorable aerodynamic conditions for the system as a whole.

As shown in Table 4, drag increases for both the leading and middle vehicles at $X_v = 2L_v$ compared to $X_v = 0.25L_v$ due to higher pressure differences between their front and rear sections. This further emphasizes the significant impact of inter-vehicle distance on the aerodynamic behavior and efficiency of high-speed multi-vehicle systems.

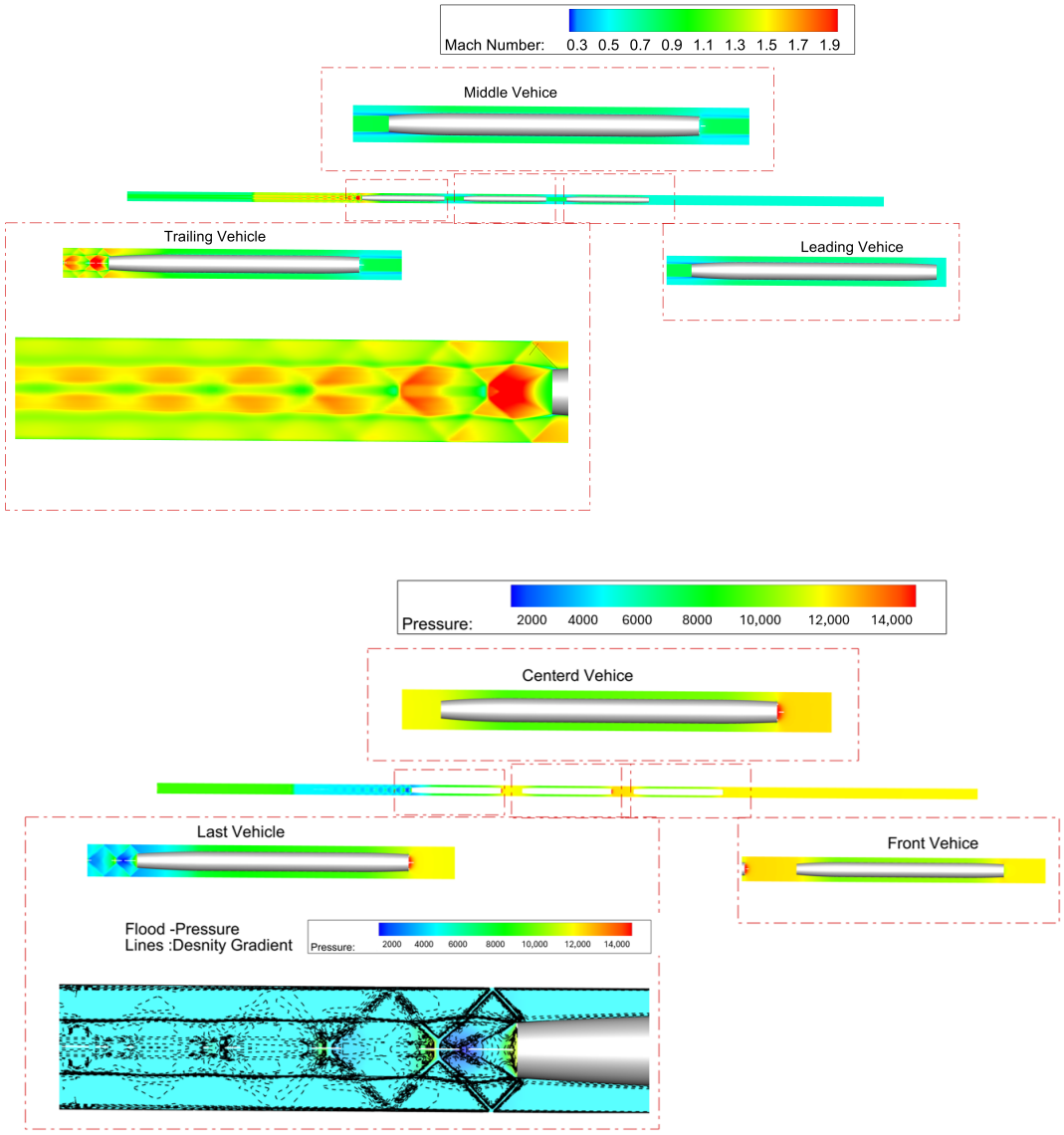

Figure 10. Mach number and static pressure contours for $X_v = 0.25L_v, M = 0.7, \beta = 0.36$.

Table 4. Thrus drag, and thrust/drag ratio for centered vehicles at various vehicle-to-vehicle distances.

Parameter	X_v	First Vehicle	Centered Vehicle	Last Vehicle	System Average
Drag (N)	$0.25L_v$	2712	3717	11,251	5893.3
	$0.5L_v$	3455	3722	11,363	6180
	$1L_v$	4394	4466	11,395	6749.6
	$2L_v$	6920	6048	11,414	8114
Thrust (N)	$0.25\ L_v$	11,478	15,476	19,000	15,318
	$0.5L_v$	11,937	16,509	21,156	16,534
	$1L_v$	13,907	14,964	19,228	16,033
	L_v	15,508	14,955	16,964	15,809
Thrust/Drag Ratio	$0.25\ L_v$	4.23	4.16	1.69	2.60
	$0.5L_v$	3.45	4.43	1.86	2.67
	$1L_v$	3.16	3.35	1.69	2.37
	$2L_v$	2.24	2.47	1.49	1.95

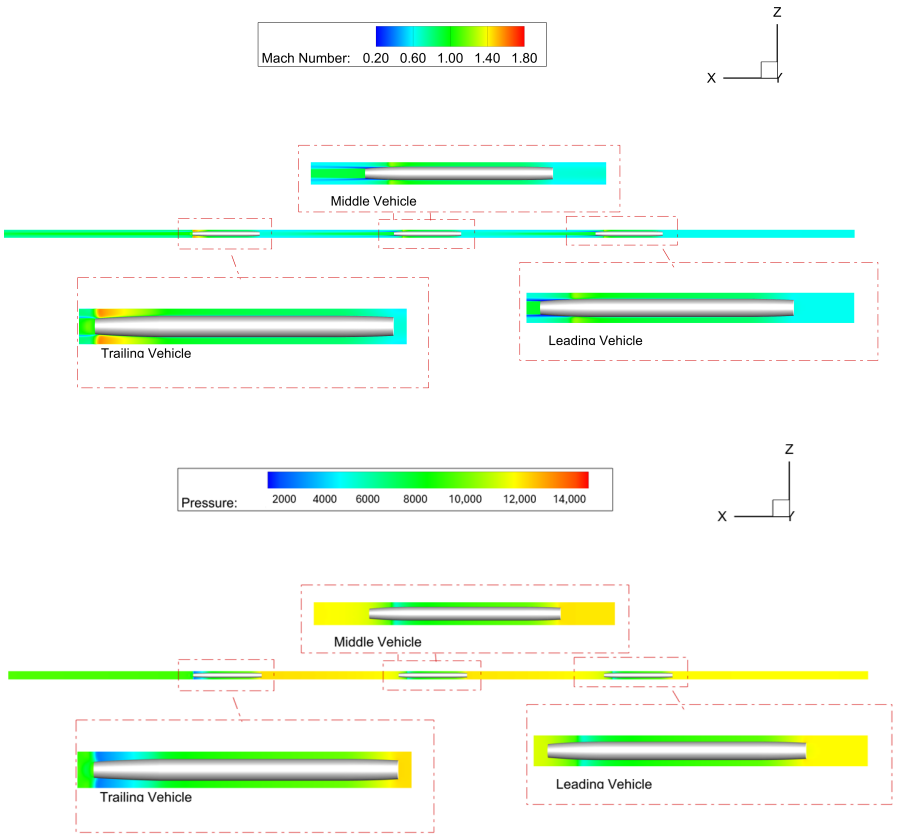

Figure 11. Static pressure and Mach number contours for $X_v = 2L_v, M = 0.7, \beta = 0.36$.

3.2.2. Drag and Thrust Analysis

Table 4 lists the values of thrust, drag, and thrust/drag ratio for centered vehicles at various vehicle-to-vehicle distances. As vehicle spacing (X_v) increases, drag on each vehicle generally rises due to the reduced influence of the trailing vehicle. This effect is especially prominent for the leading and middle (centered) vehicles, where drag increases significantly at larger spacings. For the leading vehicle, drag increases from 2712 N at $X_v = 0.25L_v$ to 6920 N at $X_v = 2L_v$. The centered vehicle shows a similar trend, with drag rising from 3717 N to 6048 N over the same spacing range. The last vehicle experiences a relatively smaller increase in drag, from 11,251 N to 11,414 N. The system achieves substantial drag reduction compared to a single vehicle, with the maximum reduction occurring at the shortest spacing ($X_v = 0.25L_v$). The average system drag at this spacing is 5893.3 N, which is significantly lower than the drag on individual vehicles at larger spacings.

Thrust generated by each vehicle also generally increases with larger spacing, though the trend is not as consistent as with drag. For example, the centered vehicle's thrust peaks at 16,509 N at $X_v = 0.5L_v$ before decreasing at larger spacings. The trailing vehicle consistently experiences higher drag than thrust, regardless of spacing. This imbalance highlights the need for additional thrust to improve the trailing vehicle's performance and contribute to system efficiency. The thrust-to-drag ratio is highest for the leading and centered vehicles at shorter distances. For instance, at $X_v = 0.25L_v$, the ratios are 4.23 and 4.16 for the first and centered vehicles, respectively. However, as spacing increases, the thrust-to-drag ratio declines for all vehicles. The trailing vehicle consistently has the lowest thrust-to-drag ratio, ranging from 1.69 to 1.49 across all spacings.

The average system performance shows promising results. The system average thrust-to-drag ratio is highest (2.67) at $X_v = 0.5L_v$, slightly better than at $X_v = 0.25L_v$ (2.60). This ratio declines to 1.95 at the largest spacing of $2L_v$. Maintaining vehicle proximity is critical to optimizing drag reduction and propulsion efficiency across the system. The data suggest

that a spacing between $0.25L_v$ and $0.5L_v$ might offer the best balance of reduced drag and improved thrust-to-drag ratio for the overall system.

3.3. System of Multiple Moving Vehicles with Suspension Effect

This section examines the aerodynamic effects of the suspension gap on flow separation, drag, thrust, shock-wave interactions, and jet inclination, providing insights into improving system efficiency in multi-vehicle configurations.

3.3.1. Flow Field Characteristics at Different Vehicle Spacings

Figures 12 and 13 illustrate the Mach number and static pressure flow field contours for two different vehicle spacings, both with a 75 mm suspension gap. Figure 12 shows the configuration for $X_v = 0.25L_v$. The trailing vehicle exhibits complex flow structures, particularly visible in the detailed flow structure view. Underexpanded jet develops behind the trailing vehicle, indicating localized flow acceleration. The flow patterns indicate three-dimensional flow complexity. The middle and leading vehicles appear to have uniform flow fields compared to the trailing vehicle. Figure 13 depicts the scenario for $X_v = 2L_v$. The overall flow field appears less disturbed compared to Figure 12. There is still a underexpanded jet behind the trailing vehicle. Again, the flow around the leading and middle vehicle is relatively uniform. The key differences between the two spacings are evident. The larger spacing in Figure 13 results in more isolated flow patterns around each vehicle. The intense flow acceleration behind the trailing vehicle is reduced with increased spacing. The interaction between vehicles appears minimized in the larger spacing configuration.

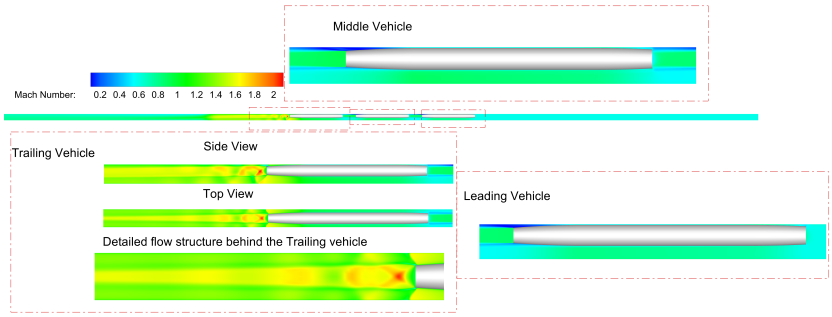

Figure 12. Mach number flow field contours with 75 mm suspension gap for $X_v = 0.25L_v$, $M = 0.7$, $\beta = 0.36$.

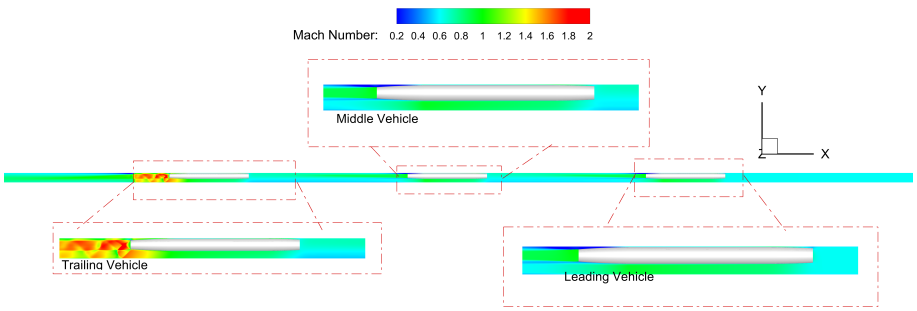

Figure 13. Mach number flow field contours with 75 mm suspension gap for $X_v = 2L_v$, $M = 0.7$, $\beta = 0.36$.

At higher Mach numbers, jet deflection due to the suspension gap significantly impacts the trailing vehicle. The deflected jet reduces thrust efficiency, as the downward-inclined flow path (caused by the Coanda effect [47]) increases turbulent mixing and drag. Numerical results indicate that, for $X_v = 0.25L_v$, the trailing vehicle experiences a thrust reduction

of approximately 12% compared to the leading vehicle, primarily due to this deflection. As vehicle spacing increases to $X_v = 2L_v$, the thrust-to-drag ratio decreases from 1.74 to 1.50, further proving that jet inclination due to the suspension gap results in a progressive decline in system efficiency.

3.3.2. Drag and Thrust Analysis

Table 5 summarizes the drag, thrust, and thrust-to-drag ratio variations across different vehicle spacings. At closer spacings ($X_v = 0.25L_v$), the system exhibits better aerodynamic performance, with drag values reaching 9497 N compared to 11,430 N at $X_v = 2L_v$. The closer spacing allows for aerodynamic shielding, reducing drag on the trailing vehicle by taking advantage of the leading vehicle's wake.

However, thrust generated by the trailing vehicle at smaller spacings is compromised by the aforementioned jet inclination, resulting in a reduced thrust-to-drag ratio of 1.74 at $X_v = 0.25L_v$. The system's thrust-to-drag ratio continues to decrease as spacing increases, with a ratio of 1.50 at $X_v = 2L_v$. This further illustrates the impact of jet inclination on overall efficiency—closer spacing helps minimize drag, but the suspension gap and resulting jet deflection create additional challenges for optimizing thrust.

Table 5. Drag thrust, and thrust-to-drag ratio for system with suspension gap included.

Parameter	X_v	First Vehicle	Centered Vehicle	Last Vehicle	Average
Drag (N)	$0.25L_v$	2712	3717	22,064	9497
	$0.5L_v$	3520	4586	22,408	10,171
	$1L_v$	4313	4760	22,932	10,668
	$2L_v$	5515	5685	23,089	11,430
Thrust (N)	$0.25L_v$	11,872	17,407	20,260	16,513
	$0.5L_v$	14,938	16,678	19,070	16,896
	$1L_v$	16,046	16,058	18,360	16,821
	$2L_v$	17,100	16,651	17,755	17,169
Thrust-to-Drag Ratio	$0.25L_v$	4.38	4.68	0.92	1.74
	$0.5L_v$	4.24	3.64	0.85	1.66
	$1L_v$	3.72	3.37	0.80	1.58
	$2L_v$	3.10	2.93	0.77	1.50

As a result, the suspension gap creates complex aerodynamic effects, with jet deflection emerging as a critical factor in reducing thrust efficiency. While closer vehicle spacings help reduce drag, the jet inclination caused by the suspension gap significantly lowers the thrust-to-drag ratio, especially for the trailing vehicle. Optimization strategies, such as adjustable nozzles or flow control mechanisms, could mitigate these effects and improve system performance.

3.4. Comparison Between the Suspended and Centered Systems

The 3D models of suspended and centered multi-vehicle Hyperloop systems are investigated at cruise conditions. The analysis focuses on pressure and Mach number distributions, shock wave interactions, and the influence of jet inclination due to suspension gaps.

3.4.1. Pressure and Mach Number Distributions

In Figure 14, the (C_p) distribution along the X-axis reveals distinct patterns for both configurations. The suspended configuration shows more pronounced fluctuations in pressure, particularly in the regions between vehicles. This is likely due to the presence of the suspension gap, which allows for complex flow interactions. In contrast, the unsuspended configuration exhibits a smoother transitions between high and low-pressure regions. In Figure 15, which focuses on the wake region of the last vehicle, we observe more detailed pressure dynamics. The "With Gap" configuration (green line) displays shock spacing. The unsuspended configuration shows a shorter shock spacing with stronger shocks. A noticable difference between the two configurations is the sharp terminating

normal shock in the unsuspended vehicle compared to the more gradual deceleration in the suspended vehicle.

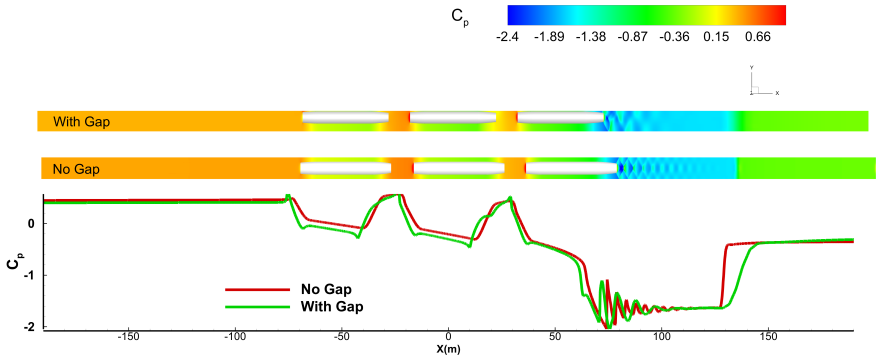

Figure 14. C_p distribution and contour plot for centered (no gap) and suspended (with gap) configurations of the multi-vehicle system (X_v = 0.25L_v, M = 0.7, β = 0.36).

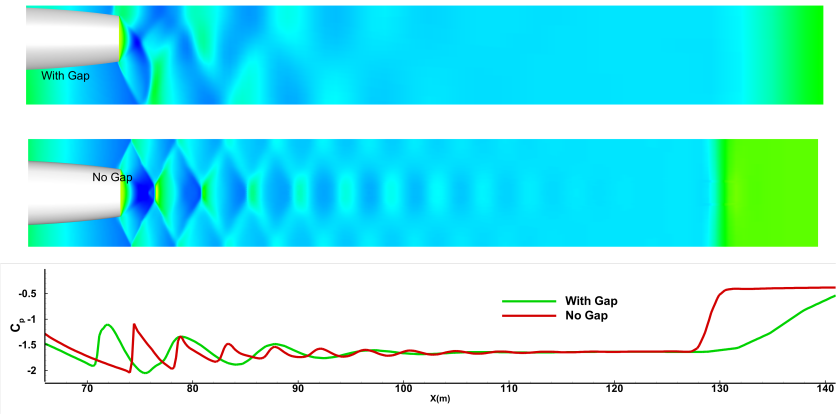

Figure 15. Flow field at the expansion region for the suspended (with gap) and centered (no gap) configurations ($X_v = 0.25L_v, M = 0.7, \beta = 0.36$).

3.4.2. Shock Wave and Jet Flow Interactions

Figures 16 and 17 demonstrate the Mach number contours for both the centered and suspended vehicle configurations. In both cases, the Mach number rapidly increases after the vehicle exit, forming a coherent jet structure that reaches Mach 2.5. As the flow moves downstream, shock diamonds form due to periodic compressions and expansions.

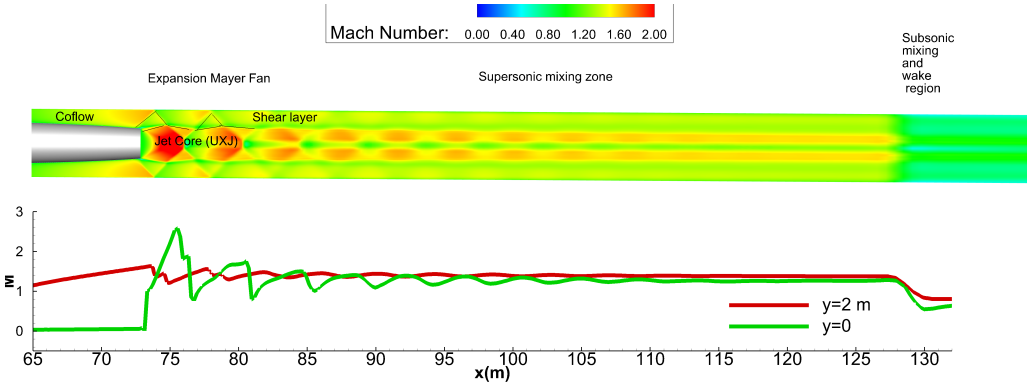

Figure 16. Flow field at the expansion region for the centered configuration of the multi-vehicle system ($X_v = 0.25L_V, M = 0.7, \beta = 0.36$).

In the suspended model (Figure 17), jet deflection due to the suspension gap becomes more pronounced. This downward deflection results in increased turbulence and asymmetric flow patterns, leading to additional shock waves and complex interactions between the jet and co-flows. These interactions create additional shear layers, further contributing to the turbulence and instability in the flow.

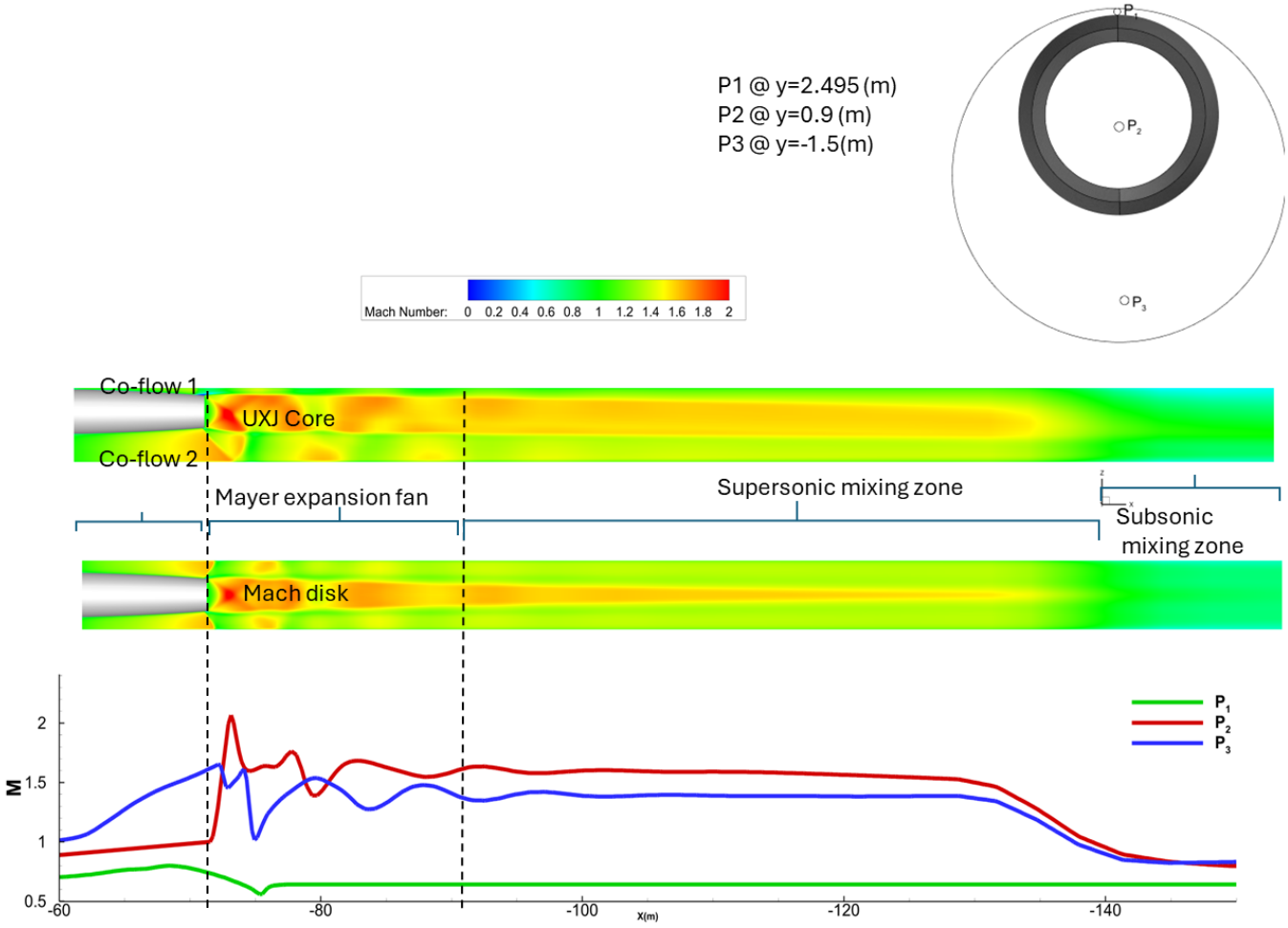

Figure 17. Flow field at the expansion region for the suspended configuration ($X_v = 0.25L_v$, $M = 0.7, \beta = 0.36$).

3.4.3. Impact of Jet Inclination on Aerodynamics

The jet inclination, influenced by the Coanda effect [47], plays a crucial role in the aerodynamic performance. The gap causes a downward deviation from the central axis, resulting in a non-uniform pressure and velocity distribution. This asymmetry extends into the subsonic mixing and wake region, where the flow takes longer to stabilize, leading to a more turbulent and dispersed wake. This affects the aerodynamic performance of subsequent vehicles in a multi-vehicle system.

The impact of jet inclination is highlighted in the Mach number distributions along three lines (P1, P2, P3) as shown in Figure 18. The downward deflection of the jet in the suspended model causes the flow to take longer to transition from supersonic to subsonic speeds (135 m vs. 125 m for the no-gap case), leading to a less efficient flow field.

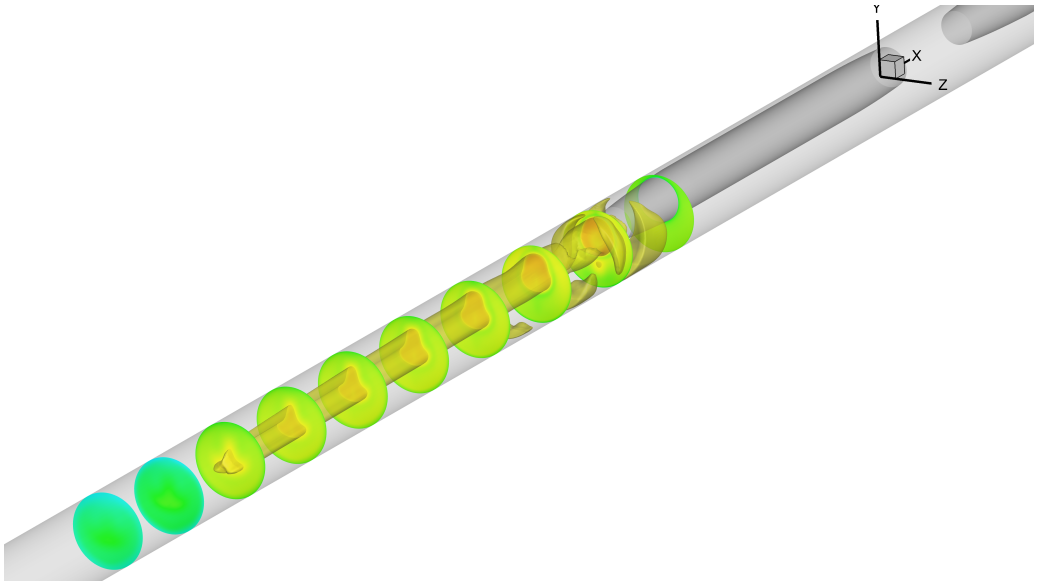

Figure 18. Mach isolines and iso-surfaces at M = 1.5 for the suspended model.

3.5. System Performance Evaluation

We evaluated the aerodynamic performance of various system configurations by measuring the drag force on each vehicle. Chart 1 shows that drag increases with larger vehicle-to-vehicle distances (X_v). All vehicles experience more drag when suspended, but this effect lessens as X_v increases.

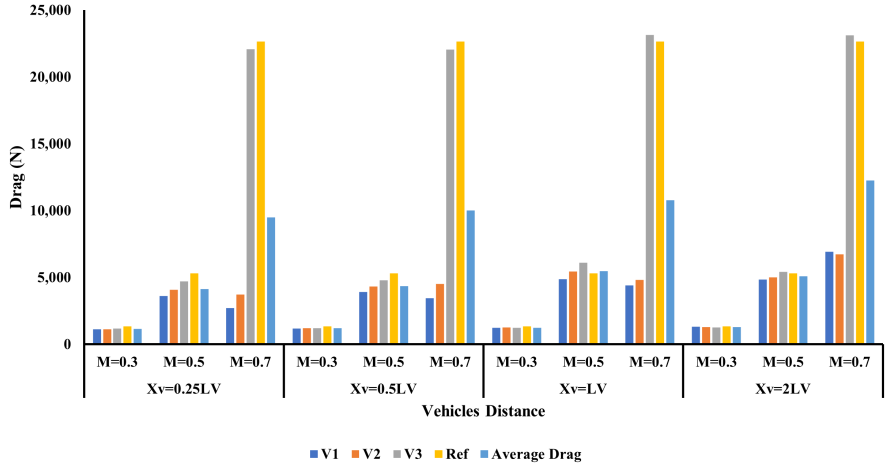

Chart 1. Drag force of each vehicle at different vehicle-to-vehicle distances.

Table 6 summarizes the drag, thrust, and T/D values for different vehicle spacings and with/without suspension. Table 7 compares the performance of two models—an axisymmetric model (without a suspension gap) and a suspended model (with a 75 mm suspension gap)—at various vehicle spacings (X_v) and Mach numbers (0.3, 0.5, and 0.7). We present key metrics, including drag and thrust for each vehicle (leading, middle, and trailing) and system-wide averages for drag reduction.

Table 6. Effect of vehicle-to-vehicle distance and suspension on drag and thrust forces for the entire system.

Parameter	$\frac{X_v}{L_v}$	Average Without Suspension (N)	Average with Suspension (N)	Increment (%)
Drag (N)	0.25	5724	9497	40%
	0.5	6035	10,171	41%
	1	6731	10,668	37%
	2	7825	11,430	38%
Thrust (N)	0.25	15,318	16,513	−7%
	0.5	16,534	16,896	−2%
	1	16,033	16,821	−4.7%
	2	15,809	17,169	−8%
Thrust-to-Drag Ratio	0.25	2.68	1.74	−35%
	0.5	2.74	1.66	−39%
	1	2.38	1.58	−34%
	2	2.02	1.50	−35%

Table 7. Performance of axisymmetric and suspended models of multiple moving vehicle hyperloop.

Axisymmetric Model (No Suspension Gap)												
	$X_v = 0.25L_V$			**$X_v = 0.5L_v$**			**$X_v = LV$**			**$X_v = 2L_v$**		
Mach	0.3	0.5	0.7	0.3	0.5	0.7	0.3	0.5	0.7	0.3	0.5	0.7
Leading Vehicle	1120	3614	2472	1163	3911	3020	1228	4871	4333	1313	4836	6920
Middle Vehicle	1118	4069	3448	1196	4320	3721	1250	5432	4465	1273	5014	6733
Trailing Vehicle	1171	4688	11,251	1199	4774	11,362	1222	6099	11,394	1260	5408	13,100.6
Ref	1326	5300	11,412	1326	5300	11,412	1326	5300	11,412	1326	5300	11,412
Average Drag	1136	4123	5723	1186	4335	6034	1233.5	5467	6731	1282	5086	8917
Average Drag/Ref. Drag (%)	86%	78%	50%	89%	82%	53%	93%	103%	59%	97%	96%	78%
Reduction	14%	25%	50%	11%	21%	47%	7%	1%	41%	3%	4%	22%
Suspended Model (with 75 mm Suspension Gap)												
Leading Vehicle	1118	3614	2711	1162	3910	3454	1227	4870	4393	1313	4836	6920
Middle Vehicle	1119	4069	3716	1196	4320	4500	1250	5432	4810	1273	5014	6733
Trailing Vehicle	1175	4688	22,062	1199	4774	22,036	1222	6099	23,129	1260	5408	23,100
Single Vehicle (Ref.)	1326	5300	22,633	1326	5300	22,633	1326.7	5300	22,633	1326	5300	22,633
Average Drag	1136	4123	9496.8	1186	4335	9997	1233.5	5467	10,778.1	1282	5086	12,251
Average Drag/Ref. Drag (%)	86%	78%	42%	89%	82%	44%	93%	103%	48%	97%	96%	54%
Reduction	14%	22%	58%	11%	18%	56%	7%	−3%	52%	3%	4%	46%

3.5.1. Drag Reduction Analysis Across Different Configurations

Axisymmetric Model (No Suspension Gap): Significant drag reduction was observed across different vehicle spacings (X_v) and Mach numbers in the axisymmetric model. The most substantial reduction occurred at the smallest spacing, $X_v = 0.25L_v$, where close

spacing between vehicles led to aerodynamic interference, reducing drag by up to 50% at Mach 0.7. This was due to favorable flow interactions, where the trailing vehicles benefited from the wake of the leading vehicles, experiencing lower drag.

However, as the spacing increased to $X_v = 2L_v$, the drag reduction dropped to 22% at Mach 0.7. With larger spacing, each vehicle was exposed to more independent airflow, decreasing the aerodynamic benefits from close proximity. This trend held consistent across other Mach numbers, although the overall drag forces were lower at Mach 0.3 and Mach 0.5.

In summary, the axisymmetric model performed most efficiently at closer spacings, where drag reduction was maximized and overall system performance improved.

Suspended Model (75 mm Suspension Gap): The suspended model, which includes a 75 mm gap, showed different drag reduction patterns. While the suspension gap introduced additional drag, especially on the trailing vehicle, the system still achieved substantial drag reduction, particularly at smaller spacings. At $X_v = 0.25L_v$ and Mach 0.7, the suspended model saw a drag reduction of 58%, even higher than the axisymmetric model, despite the added complexity of the suspension gap.

As in the axisymmetric model, drag reduction decreased with larger spacings. At $X_v = 2L_v$, the reduction was 46% at Mach 0.7, still higher than the 22% reduction in the axisymmetric model at the same spacing. The suspension gap's more complex flow interactions likely explain this.

Across all Mach numbers, the suspended model showed a similar pattern of drag reduction, though the gap's impact was more noticeable at higher Mach numbers, where the flow disturbances were more pronounced.

When comparing both configurations, the axisymmetric model generally exhibited better performance, with lower drag forces and higher efficiency, particularly at larger vehicle spacings. However, the suspended model performed better at close spacings, despite its increased drag due to the suspension gap.

Overall, minimizing vehicle spacing was key to maximizing drag reduction in both configurations. The axisymmetric model remains more efficient, especially as spacing increases, while the suspended model benefits from higher drag reduction at closer distances but suffers from higher drag penalties due to the gap.

Chart 1 illustrates the drag forces on each vehicle at various vehicle-to-vehicle distances. In the axisymmetric model, the trailing vehicle experiences the highest drag. The maximum average drag reduction occurs at $X_v = 0.25L_v$ and Mach 0.7. As X_v increases, drag reduction decreases, with the smallest reduction being 41%. At lower Mach numbers, the difference in drag reduction across spacings is less pronounced.

Chart 2 shows that suspended vehicles generate slightly more thrust compared to non-suspended ones, with thrust increasing as X_v grows. For both the leading and middle vehicles, thrust exceeds drag, but the trailing vehicle experiences higher drag. This suggests that a traction mechanism could help pull the trailing vehicle, reducing energy consumption.

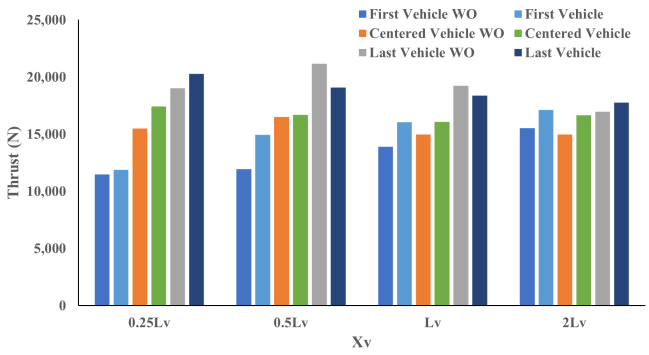

Chart 2. Thrust force generated by each vehicle at different vehicle-to-vehicle distances.

3.5.2. Thrust-to-Drag Ratio

The inclusion of a suspension gap results in a significant decrease in the thrust-to-drag ratio (T/D). For example, at $X_v = 0.25L_v$, the T/D drops by 35%, from 2.68 in the axisymmetric model to 1.74 in the suspended model. As X_v increases, the T/D continues to decline, indicating that the suspension gap has a larger negative impact on drag than it does on thrust. The drop in T/D is more pronounced at closer vehicle spacings, but it persists across all configurations, reducing aerodynamic efficiency.

Table 6 summarizes the drag, thrust, and T/D values for different vehicle spacings and with/without suspension.

3.5.3. Energy Efficiency Implications

The T/D and drag reduction significantly impact the energy efficiency of the Hyperloop system. Configurations that reduce drag and maintain high T/D values are more energy efficient. In the axisymmetric model, closer vehicle spacings ($X_v = 0.25L_v$) significantly reduce drag and keep T/D values high, leading to lower energy consumption. In contrast, the suspended model, with its 75 mm suspension gap, has much lower T/D values (e.g., 0.92 at $X_v = 0.25L_v$ and Mach 0.7), resulting in higher energy demands. As spacing increases, the energy inefficiency becomes more pronounced in the suspended model due to increased drag and reduced T/D, making it less energy efficient than the axisymmetric model. Minimizing vehicle spacing and addressing the aerodynamic penalties from the suspension gap are critical to improving the energy efficiency of Hyperloop systems.

4. Conclusions

This study provides a comprehensive analysis of the aerodynamic performance of a multi-vehicle Hyperloop system propelled by jets within a low-pressure tube. The analysis included two configurations: an axisymmetric model without suspension gaps and a suspended model with a 75 mm gap. The performance of these configurations was assessed at Mach numbers of 0.3, 0.5, and 0.7, with particular focus on the effects of vehicle spacing and suspension gaps on drag, thrust, and flow characteristics. Numerical simulations were conducted using the Reynolds-Averaged Navier–Stokes (RANS) equations, validated by the DLR hydrogen ejector model and the RAE 2822 airfoil case.

The flow structure around the vehicles revealed significant differences between single and multiple vehicle configurations. The presence of suspension gaps notably influenced the flow patterns, particularly at higher Mach numbers (0.7), resulting in complex interactions between compression and expansion waves. The 75 mm suspension gap demonstrated a pronounced effect, leading to a downward jet inclination, increased turbulence, and more complex flow structures. This inclination negatively impacted the flow transition from supersonic to subsonic speeds, contributing to increased drag on the trailing vehicle. The main findings highlight the following:

1. Vehicle Spacing's Impact on Drag Reduction: The results show that closer vehicle spacing significantly reduces aerodynamic drag, particularly at higher Mach numbers. At the smallest spacing ($X_v = 0.25L_v$), drag was reduced by up to 58% in the suspended model at Mach 0.7, indicating that optimizing vehicle spacing is crucial for improving system efficiency. The axisymmetric model showed an average drag reduction between 14% and 50%, depending on Mach numbers and spacings, with maximum drag reduction occurring at Mach 0.7 and $X_v = 0.25L_v$.
2. Effect of Suspension Gaps: The inclusion of a 75 mm suspension gap introduced additional drag, especially on the trailing vehicle, due to jet deflection and flow asymmetry. While drag reduction was still achieved, particularly at smaller spacings, the overall thrust-to-drag ratio decreased compared to the axisymmetric model without gaps. At certain configurations, such as Mach 0.5 and $0.5L_v$, a negative drag reduction (-3%) was observed, indicating that suspension gaps must be carefully managed to avoid performance degradation.

3. Thrust-to-Drag Ratio and Energy Efficiency: The axisymmetric configuration, without suspension gaps, demonstrated the highest energy efficiency, particularly at smaller spacings. In contrast, the suspended model showed lower thrust-to-drag ratios due to the increased drag caused by the suspension gap, impacting overall energy consumption. However, at Mach 0.7 and a vehicle spacing of L_v, the suspended model showed a maximum drag reduction of 52%, exceeding the axisymmetric configuration.

These findings underscore the importance of minimizing vehicle spacing in Hyperloop systems to reduce drag and improve energy efficiency. The research also highlights the challenges posed by suspension gaps, which, while necessary for practical vehicle design, require further optimization to maintain high aerodynamic performance. Unsteady simulations, such as Large Eddy Simulation (LES) or Detached Eddy Simulation (DES), are recommended for future research to better capture the complex transient wake interactions between vehicles. Additionally, implementing advanced methods like Cascade Ensemble Learning (CEL) could provide deeper insights into multi-level interactions between vehicles in confined low-pressure environments, further optimizing the system's aerodynamic performance and efficiency.

Author Contributions: Conceptualization, S.A. and M.M.A.; Methodology, K.J.; Validation, M.M.A.; Formal analysis, I.A.; Investigation, S.A. and M.M.A.; Writing—original draft, S.A. and M.M.A.; Writing—review & editing, S.A., M.M.A. and I.A.; Supervision, I.A. and K.J.; Funding acquisition, K.J. All authors have read and agreed to the published version of the manuscript.

Funding: This project was funded by the Deanship of Scientific Research (DSR) at King Abdulaziz University, Jeddah, under Grant No. (GPIP: 11-135-2024). The authors, therefore, acknowledge with thanks DSR for technical and financial support.

Institutional Review Board Statement: Not applicable.

Informed Consent Statement: Not applicable.

Data Availability Statement: The data that support the findings of this study are available upon reasonable request from the authors.

Acknowledgments: The authors gratefully acknowledge the High-Performance Computing Center (Aziz Supercomputer) at King Abdulaziz University (https://hpc.kau.edu.sa/Default-611997-EN) for assisting with the simulations and analysis for this study.

Conflicts of Interest: The authors declare no conflicts of interest.

List of Abbreviations

A_v	Vehicle area
A_{tube}	Tube area
a	Speed of sound
D	Drag force
D_v	Vehicle diameter
dt	Time step
L_v	Vehicle length
M	Mach number
$\dot{m}$	Mass flow rate
P	Operating pressure
R	Gas constant
V	Vehicle velocity
X_v	Vehicle-to-vehicle distance
β	Blockage ratio = $\frac{A_v}{A_{tube}}$
γ	$\frac{c_p}{c_v}$ = 1.4 for ideal air
ρ	Flow density

References

1. Foa, J.V. *An Introduction to Project Tubeflight*; Rensselaer Polytechnic Institute: Troy, NY, USA, 1966. Available online: https://dspace.rpi.edu/handle/20.500.13015/25 (accessed on 22 October 2024).
2. Oster, D.; Kumada, M.; Zhang, Y. Evacuated tube transport technologies (ET3)tm: A maximum value global transportation network for passengers and cargo. *J. Mod. Transp.* **2011**, *19*, 42–50. [CrossRef]
3. Musk, E. Hyperloop Alpha. SpaceX. 2013. Available online: https://www.spacex.com/sites/spacex/files/hyperloop_alpha.pdf (accessed on 22 October 2024).
4. Kim, T.K.; Kim, K.H.; Kwon, H.B. Aerodynamic characteristics of a tube train. *J. Wind. Eng. Ind. Aerodyn.* **2011**, *99*, 1187–1196. [CrossRef]
5. Le, T.T.G.; Jang, K.S.; Lee, K.S.; Ryu, J. Numerical Investigation of Aerodynamic Drag and Pressure Waves in Hyperloop Systems. *Mathematics* **2020**, *8*, 1973. [CrossRef]
6. HAMMITT, A.G. Aerodynamic analysis of tube vehicle systems. *AIAA J.* **1972**, *10*, 282–290. [CrossRef]
7. Abdulla, M.; Juhany, K.A. A Rapid Solver for the Prediction of Flow-Field of High-Speed Vehicle Moving in a Tube. *Energies* **2022**, *15*, 6074. [CrossRef]
8. Yang, Y.; Wang, H.; Benedict, M.; Coleman, D. Aerodynamic Simulation of High-Speed Capsule in the Hyperloop System. In Proceedings of the 35th AIAA Applied Aerodynamics Conference, Denver, CO, USA, 5–9 June 2017. [CrossRef]
9. Zhang, Y. Numerical simulation and analysis of aerodynamic drag on a subsonic train in evacuated tube transportation. *J. Mod. Transp.* **2012**, *20*, 44–48. [CrossRef]
10. Kang, H.; Jin, Y.; Kwon, H.; Kim, K. A Study on the Aerodynamic Drag of Transonic Vehicle in Evacuated Tube Using Computational Fluid Dynamics. *Int. J. Aeronaut. Space Sci.* **2017**, *18*, 614–622. [CrossRef]
11. Oh, J.S.; Kang, T.; Ham, S.; Lee, K.S.; Jang, Y.J.; Ryou, H.S.; Ryu, J. Numerical Analysis of Aerodynamic Characteristics of Hyperloop System. *Energies* **2019**, *12*, 518. [CrossRef]
12. Gillani, S.A.; Panikulam, V.P.; Sadasivan, S.; Yaoping, Z. CFD Analysis of Aerodynamic Drag Effects on Vacuum Tube Trains. *J. Appl. Fluid Mech.* **2019**, *12*, 303–309. [CrossRef]
13. Le, T.T.G.; Kim, J.; Jang, K.S.; Lee, K.S.; Ryu, J. Numerical study of unsteady compressible flow induced by multiple pods operating in the Hyperloop system. *J. Wind. Eng. Ind. Aerodyn.* **2022**, *226*, 105024. [CrossRef]
14. Niu, J.; Sui, Y.; Yu, Q.; Cao, X.; Yuan, Y. Numerical study on the impact of Mach number on the coupling effect of aerodynamic heating and aerodynamic pressure caused by a tube train. *J. Wind. Eng. Ind. Aerodyn.* **2019**, *190*, 100–111. [CrossRef]
15. Thorley, A.; Tiley, C. Unsteady and transient flow of compressible fluids in pipelines—A review of theoretical and some experimental studies. *Int. J. Heat Fluid Flow* **1987**, *8*, 3–15. [CrossRef]
16. Lluesma-Rodríguez, F.; González, T.; Hoyas, S. CFD Simulation of a Hyperloop Capsule Inside a Low-Pressure Environment Using an Aerodynamic Compressor as Propulsion and Drag Reduction Method. *Appl. Sci.* **2021**, *11*, 3934. [CrossRef]
17. Kwon, H.; Jin, Y.; Lee, W.; Kang, H. The Feasibility of Adapting Air Compressor to a High-Speed Train to Attenuate the Aerodynamic Problems in Tunnel. *Int. J. Aeronaut. Space Sci.* **2020**, *21*, 638–646. [CrossRef]
18. Bizzozero, M.; Sato, Y.; Sayed, M.A. Aerodynamic study of a Hyperloop pod equipped with compressor to overcome the Kantrowitz limit. *J. Wind. Eng. Ind. Aerodyn.* **2021**, *218*, 104784. [CrossRef]
19. Lee, H.W.; Kim, K.C.; Lee, J. Review of maglev train technologies. *IEEE Trans. Magn.* **2006**, *42*, 1917–1925. [CrossRef]
20. Jang, K.S.; Le, T.T.G.; Kim, J.; Lee, K.S.; Ryu, J. Effects of compressible flow phenomena on aerodynamic characteristics in Hyperloop system. *Aerosp. Sci. Technol.* **2021**, *117*, 106970. [CrossRef]
21. Kim, J.; Jang, K.S.; Le, T.T.G.; Lee, K.S.; Ryu, J. Theoretical and numerical analysis of pressure waves and aerodynamic characteristics in Hyperloop system under cracked-tube conditions. *Aerosp. Sci. Technol.* **2022**, *123*, 107458. [CrossRef]
22. Hu, X.; Deng, Z.; Zhang, J.; Zhang, W. Effect of tracks on the flow and heat transfer of supersonic evacuated tube maglev transportation. *J. Fluids Struct.* **2021**, *107*, 103413. [CrossRef]
23. Opgenoord, M.M.J.; Caplan, P.C. Aerodynamic Design of the Hyperloop Concept. *Aiaa J.* **2018**, *56*, 4261–4270. [CrossRef]
24. Braun, J.; Sousa, J.; Pekardan, C. Aerodynamic Design and Analysis of the Hyperloop. *Aiaa J.* **2017**, *55*, 4053–4060. [CrossRef]
25. Lluesma-Rodríguez, F.; González, T.; Hoyas, S. CFD simulation of a hyperloop capsule inside a closed environment. *Results Eng.* **2021**, *9*, 100196. [CrossRef]
26. Mirza, M.O.; Ali, Z. Numerical analysis of aerodynamic characteristics of multi-pod hyperloop system. *Proc. Inst. Mech. Eng. Part J. Aerosp. Eng.* **2023**, *237*, 1727–1750. [CrossRef]
27. Nick, N.; Sato, Y. Computational fluid dynamics simulation of Hyperloop pod predicting laminar–turbulent transition. *Railw. Eng. Sci.* **2020**, *28*, 97–111. [CrossRef]
28. Le, T.T.G.; Kim, J.; Cho, M.; Ryu, J. Effects of tail shapes/lengths of Hyperloop pod on aerodynamic characteristics and wave phenomenon. *Aerosp. Sci. Technol.* **2022**, *131*, 107962. [CrossRef]
29. Zhou, K.; Ding, G.; Wang, Y.; Niu, J. Aeroheating and aerodynamic performance of a transonic hyperloop pod with radial gap and axial channel: A contrastive study. *J. Wind. Eng. Ind. Aerodyn.* **2021**, *212*, 104591. [CrossRef]
30. THE LINE: A Revolution in Urban Living. Available online: https://www.neom.com/en-us/regions/theline (accessed on 22 October 2024).
31. Alzhrani, S.; Abdulla, M.; Juhany, K.A.; AlQadi, I. Effect of Maglev Suspension on the Aerodynamics of Multiple Vehicles Moving in a Low-Pressure Tube. *J. Physics Conf. Ser.* **2024**, *2772*, 012013. [CrossRef]

32. Kim, J.; Lee, C.; Le, T.T.G.; Kim, D.; Won, Y.; Cho, M.; Ryu, J. Effects of eccentricity in tube–pod arrangements on hyperloop aerodynamics. *Int. J. Mech. Sci.* **2024**, *279*, 109505 [CrossRef]
33. Zhou, P.; Qin, D.; Zhang, J.; Li, T. Aerodynamic characteristics of the evacuated tube maglev train considering the suspension gap. *Int. J. Rail Transp.* **2022**, *10*, 195–215. [CrossRef]
34. Abdulla, M.; Alzhrani, S.; Juhany, K.A.; AlQadi, I. Application of Adjoint Aerodynamics Optimization for a High-Speed Vehicle Moving in a Tube. *J. Physics Conf. Ser.* **2024**, *2772*, 012012. [CrossRef]
35. Alzhrani, S.; Abdulla, M.M.; Juhany, K.A.; AlQadi, I. Aerodynamics Performance of Air-Breathing Multiple-Vehicle Hyperloop System. *Arab. J. Sci. Eng.* **2024**, *49*, 11215–11232. [CrossRef]
36. Abdulla, M.M.; Alzhrani, S.; Juhany, K.A.; Abdulla, M.; Alzhrani, S.; Juhany, K.A. Aerodynamics Analysis of Vehicle Moving in a Tube. In Proceedings of the HiSST: 2nd International Conference on High-Speed Vehicle Science Technology, Bruges, Belgium, 11–16 September 2022; pp. 11–15.
37. Chen, X.; Zhao, L.; Ma, J.; Liu, Y. Aerodynamic simulation of evacuated tube maglev trains with different streamlined designs. *J. Mod. Transp.* **2012**, *20*, 115–120. [CrossRef]
38. Menter, F.R. Two-equation eddy-viscosity turbulence models for engineering applications. *Aiaa J.* **1994**, *32*, 1598–1605. [CrossRef]
39. Barth, T.; Jespersen, D. The design and application of upwind schemes on unstructured meshes. In Proceedings of the 27th Aerospace Sciences Meeting, Reno, NV, USA, 9–12 January 1989; American Institute of Aeronautics and Astronautics: Reston, VA, USA, 1989. [CrossRef]
40. Roe, P.L. Approximate Riemann Solvers, Parameter Vectors, and Difference Schemes. *J. Comput. Phys.* **1997**, *135*, 250–258. [CrossRef]
41. Oßwald, K.; Siegmund, A.; Birken, P.; Hannemann, V.; Meister, A. L2Roe: A low dissipation version of Roe's approximate Riemann solver for low Mach numbers. *Int. J. Numer. Methods Fluids* **2016**, *81*, 71–86. [CrossRef]
42. Aziz Hpcc | and Supercomputer. 2024. Available online: https://hpc.kau.edu.sa/Default-611997-EN (accessed on 22 October 2024).
43. Xue, R.; Wei, X.; He, G.; Hu, C.; Tang, X. Effect of parallel-jet addition on the shock train characteristics in a central-strut isolator by detached eddy simulation. *Int. J. Heat Mass Transf.* **2017**, *114*, 1159–1168. [CrossRef]
44. Cook, P.H.; Firmin, M.C.P.; McDonald, M.A.; Establishment, R.A. *Aerofoil RAE 2822: Pressure Distributions, and Boundary Layer and Wake Measurements*; North Atlantic Treaty Organization, Advisory Group for Aerospace Research and Development: Ottawa, ON, Canada, 1979; p. 606.
45. Spalart, P.; Allmaras, S. A one-equation turbulence model for aerodynamic flows. In Proceedings of the 30th Aerospace Sciences Meeting and Exhibit, Reno, NV, USA, 6–9 January 1992; American Institute of Aeronautics and Astronautics: Reston, VA, USA, 1992. [CrossRef]
46. Chien, K.Y. Predictions of Channel and Boundary-Layer Flows with a Low-Reynolds-Number Turbulence Model. *AIAA J.* **2012**, *20*, 33–38. [CrossRef]
47. Matsuo, S.; Setoguchi, T.; Kudo, T.; Yu, S. Study on the characteristics of supersonic Coanda jet. *J. Therm. Sci.* **1998**, *7*, 165–175. [CrossRef]